Master of Science in Neuroscience

# Quantitative predictions of cerebral arterial labeling employing neural network ensemble orchestrate precise investigation in brain frailty of cerebrovascular disease

February 2023

Graduate School of Natural Sciences
Seoul National University
Brain Science Major

SukWoo Hong

# Quantitative predictions of cerebral arterial labeling employing neural network ensemble orchestrate precise investigation in brain frailty of cerebrovascular disease

지도교수 김 상 윤

이 논문을 이학석사 학위논문으로 제출함

2022 년 11 월

서울대학교 대학원

협동과정 뇌과학전공

홍 석 우

홍석우의 석사 학위논문을 인준함

2023년 1 월

위 원 장 _____ 한문구

부위원장 _____ 김상윤

위 원 _____ 서우근

# Quantitative predictions of cerebral arterial labeling employing neural network ensemble orchestrate precise investigation in brain frailty of cerebrovascular disease

by

*SukWoo Hong[1,2], †WooKeun Seo[2,3], †SangYun Kim[1,4]

A master's thesis submitted to the faculty of the Program in Brain Science
in partial fulfillment of the requirements for the
Master of Science in Neuroscience

The undersigned have examined this dissertation and, at this moment, certify that it is worthy of acceptance for a master's degree from Seoul National University.

1. Program in Brain Science, College of Natural Sciences, Seoul National University, Seoul 08826, Korea
2. Department of Neurology and Stroke Center, Samsung Medical Center, Sungkyunkwan University School of Medicine, Seoul 06351, Korea
3. Department of Digital Health, Samsung Advanced Institute for Health Sciences & Technology, Sungkyunkwan University School of Medicine, Seoul 06351, Korea
4. Department of Neurology, Seoul National University College of Medicine & Clinical Neuroscience Center, Seoul National University Bundang Hospital, Seongnam-si 13620, Korea

February 2023

| | | |
|---|---|---|
| Committee Chair | MoonKu Han, M.D., Ph.D.[4] | ( ) |
| Committee Co-chair | †SangYun Kim, M.D., Ph.D.[1,4] | ( ) |
| Vice Chair | †WooKeun Seo, M.D., Ph.D.[2,3] | ( ) |

# Acronym

ICA, internal carotid arteries; OA, ophthalmic arteries; ACHA, anterior choroidal arteries; VA, ver-tebral arteries; PICA, posterior inferior cerebellar arteries; AICA, anterior inferior cerebellar arter-ies; IAA, internal auditory arteries; SCA, superior cerebellar arteries; PCOA, posterior communi-cating arteries; PCA, posterior cerebral arteries; P1, pre-communicating PCA; P2, post-communicating PCA; P1P2, merging of P1 and P2; P3P4, mixture of quadrigeminal and calcarine PCA; PO, parieto-occipital arteries; PCALC, calcarine arteries; PPA, direct peduncular perforating ar-teries; H.A., hippocampal arteries; PCAAT, anterior temporal PCA; PCAPT, posterior temporal PCA; PCALP, lateral posterior choroidal arteries; M1, sphenoidal middle cerebral artery; MCA, middle cerebral arteries; MCAS, superior division of MCA; MCAI, inferior division of MCA; MCALO, lateral orbitofrontal arteries; MCAPR, pre-Rolandic MCA; MCAR, Rolandic MCA; MCAAP, anterior parietal MCA; MCAPP, posterior parietal MCA; MCAA, angular MCA; MCAPT, posterior temporal MCA; MCAMT, middle temporal MCA; MCAAT, anterior temporal MCA; MCAPF, pre-frontal MCA; ACA, anterior cerebral arteries; A1, horizontal pre-communicating ACA; A2, vertical post-communicating pre-callosal ACA; A1A2, combination of A1 and A2; ACAMO, medial orbitofrontal ACA; A2F, fron-topolar vertical post-communicating pre-callosal ACA; ACAC, callosomarginal ACA; ACAP, pericallosal ACA; B.A., basilar artery; ACOA, anterior communicating artery; A0, anterior communicating artery; A1, branches of the right internal carotid arteries; A2, branches of the left internal carotid arteries; A3, basal branches of the right middle cere-bral artery; A4, basal branches of the left middle cerebral artery; A5, basal branches of the right anterior cerebral artery; A6, basal branches of the left anterior cerebral artery; A7, pial branches of the right middle cerebral artery; A8, pial branches of the left middle cerebral artery; A9, pial branches of the right anterior cerebral artery; A10, pial branches of the left anterior cerebral artery; P0, basilar artery; P1, branches of the right vertebral artery; P2, branches of the left vertebral artery; P3, basal branches of the right posterior cerebral artery; P4, basal branches of the left posterior cere-bral artery; P5, pial branches of the right posterior cerebral artery; P6, pial branches of the right posterior cerebral artery; P7, branches of the right superior cerebellar artery, anterior inferior cerebellar artery, and posterior inferior cerebellar artery; P8, branches of the left superior cerebellar artery, anterior inferior cerebellar artery, and posterior inferior cerebellar artery

# Abstract

Identifying the cerebral arterial branches is essential for undertaking a computational approach to cerebrovascular imaging. However, the complexity and inter-individual differences involved in this process have not been thoroughly studied. We used machine learning to examine the anatomical profile of the cerebral arterial tree. The method is less sensitive to inter-subject and cohort-wise anatomical variations and exhibits robust performance with an unprecedented in-depth vessel range.

We applied machine learning algorithms to disease-free healthy control subjects ($n$ = 42), patients with stroke with intracranial atherosclerosis (ICAS) ($n$ = 46), and patients with stroke mixed with the existing controls ($n$ = 69). We trained and tested 70% and 30% of each study cohort, respectively, incorporating spatial coordinates and geometric vessel feature vectors. Cerebral arterial images were analyzed based on the 'segmentation-stacking' method using magnetic resonance angiography. We precisely classified the cerebral arteries across the exhaustive scope of vessel components using advanced geometric characterization, redefinition of vessel unit conception, and post-processing algorithms. We verified that the neural network ensemble, with multiple joint models as the combined predictor, classified all vessel component types independent of inter-subject variations in cerebral arterial anatomy. The validity of the categorization performance of the model was tested, considering the control, ICAS, and control-blended stroke cohorts, using the area under the receiver operating characteristic (ROC) curve and precision-recall curve.

The classification accuracy rarely fell outside each image's 90–99% scope, independent of cohort-dependent cerebrovascular structural variations. The classification ensemble was calibrated with high overall area rates under the ROC curve of 0.99–1.00 [0.97–1.00] in the test set across various study cohorts. Identifying an all-inclusive range of vessel components across controls, ICAS, and stroke patients, the accuracy rates of the prediction were: internal carotid arteries, 91–100%; middle cerebral arteries, 82–98%; anterior cerebral arteries, 88–100%; posterior cerebral arteries, 87–100%; and collections of superior, anterior inferior, and posterior inferior cerebellar arteries, 90–99% in the chunk-level classification. Using a voting algorithm on the queued classified vessel factors and anatomically post-processing the automatically classified results intensified quantitative prediction performance.

We employed stochastic clustering and deep neural network ensembles. Machine

intelligence-assisted prediction of vessel structure allowed us to personalize quantitative predictions of various types of cerebral arterial structures, contributing to precise and efficient decisions regarding cerebrovascular disease.

**Keyword:** cerebrovascular disorders, stroke, neuropathogenesis, computer reasoning, machine intelligence, patient-specific modeling, computational biology, early diagnosis, precision medicine

**Student Identification Number:** 2021-20355

# Table of Contents

# List of Figures

# List of Tables

# Chapter 1. Automated in-depth cerebral arterial labeling using cerebrovascular vasculature reframing and deep neural networks

*Automated cerebral arterial labeling*

## 1.1. Introduction

Defining the morphological nature of cerebral circulation and providing quantified information, so-called digitization, are the indispensable hallmark of identifying pathogenic mechanisms, diagnosing disease, and determining the clinical relevance of cerebrovascular dysfunctions. Automated labeling of the major cerebral arterial branch is the first step for quantitatively analyzing cerebral arterial morphology from cerebrovascular images. Previous progressions include atlas-based artery identification and post-processing improvement using iterative region-growing territorial expansion.[1-3] Characterising the considerable variations in complex intracranial vascular structures, half of which are usually located outside the Circle of Willis, has been challenging but is a crucial step in quantifying structural information of the cerebrovasculature.[4] Previously suggested methods of automated identification of major cerebral vascular territories have suffered from practical limitations attributable to complexities and inter-individual variabilities of the cerebrovasculature. Therefore, these methods covered only the major branches of the Circle of Willis for automated labelling.[1-3]

Here, we overcome the problems mentioned above, leveraging geometric features obtained from systematic time-of-flight magnetic resonance angiography (TOF MRA) with a deep neural network and advanced the performance of the models by reorganizing vascular units for clinically disparate personalized cerebral vessel modules.

This study aimed to segment the cerebrovascular arterial branches in a fully automatic manner. We focused on cerebral arterial circuits, systematizing and validating neural network models to render them clinically pragmatic.

## 1.2. Materials and methods

### 1.2.1. Study design and subjects

The study subjectsd In accordance with the primary purpose of this study which was the development of an automated cerebral arterial labeling algorithm, we used a pre-established cohort retrospectively. The study subjects were healthy controls, stroke patients, and stroke patients with intracranial atherosclerosis (ICAS) over 20 years (Figure 1).

The control cohorts for the algorithm development were healthy subjects who visited the comprehensive health promotion centre at the Samsung Medical Center and who underwent MRA from January 1, 2013, to December 31, 2013, excluding those who had the following: (i) stroke including ischemic stroke, hemorrhagic stroke, and transient ischemic attack; (ii) coronary artery or heart disease; (iii) ICAS; (iv) intracranial arterial anomalies corresponding to pathological conditions or variants of normal anatomy; (v) congenital morbidity including cerebral arterial hypoplasia; and (vi) miscellaneous abnormal cases diagnosed by angiography.

Stroke patients for the external validation of the algorithm were selected from the Samsung Medical Center stroke registry (SMC stroke registry). This prospectively collected stroke registry recruited acute stroke patients seven days after stroke onset. Another specially selected stroke group was intended to provide clinical relevance to the algorithm from the patients who participated in The Intensive Statin Treatment in Acute Ischemic Stroke Patients with Intracranial Atherosclerosis - High-Resolution Magnetic Resonance Imaging (STAMINA-MRI) study[5] with significant and symptomatic intracranial arterial stenosis of > 50% in the middle cerebral artery of the basilar artery.

Demographic data and vascular risk factors were collected from the medical records for controls and the stroke registry for the stroke cohort.

The Samsung Medical Center Institutional Review Board approved the study design (SMC-2021-04-072). This study was performed in accordance with the declaration of Helsinki. Informed consent was waived by the Samsung Medical Center Institutional Review Board for the control group because the study progressed in a retrospective manner, and we provided the clinical data and brain images in an anonymized form. Written informed consent was obtained from those enrolled in the SMC stroke registry.

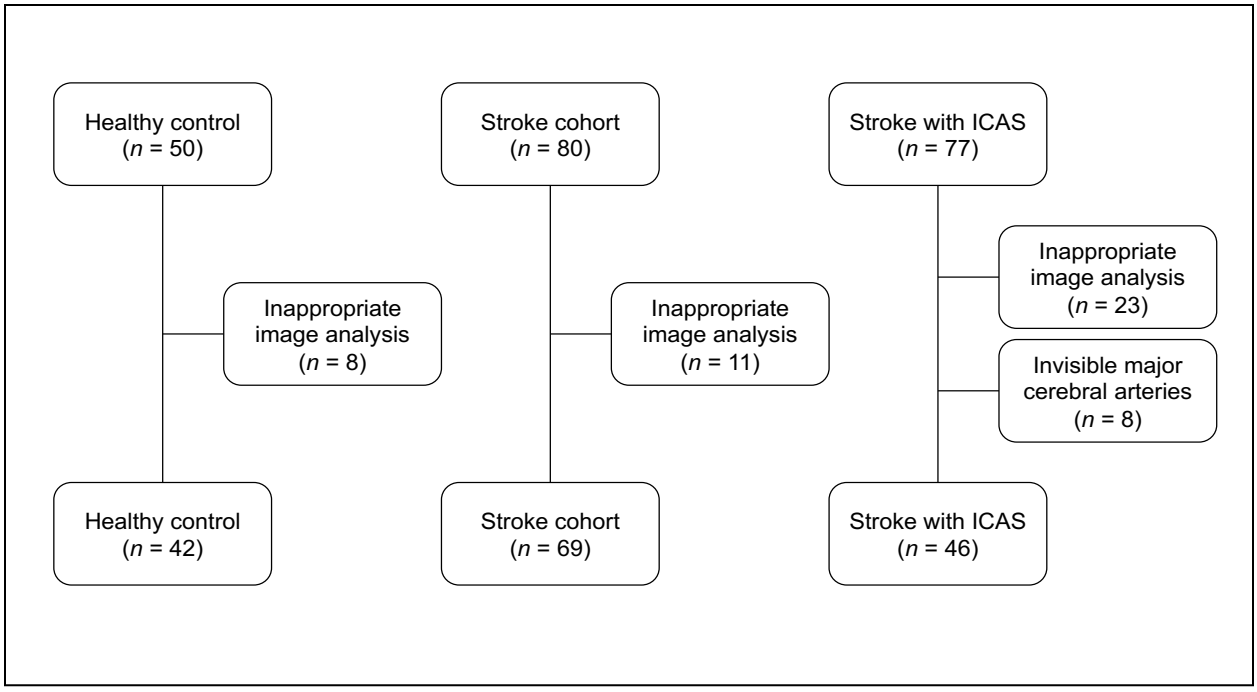


**Figure 1. Inclusion flow chart of study cohorts.**

Rationales of non-participation of study subjects excluded in each cohort.

## 1.2.2. Imaging preparation

### 1.2.2.1. Magnetic resonance machine

The intracranial arteries were imaged using a 3.0 T Philips Achieva magnetic resonance imaging scanner (Philips Medical Systems) equipped with a 32-element phased-array receiver head coil.

### 1.2.2.2. Magnetic resonance sequence

This study used whole-brain three-dimensional (3D) MRA images with a TOF protocol collected from each participant. With an isotropic voxel size configured to 0.284 × 0.284 $mm^3$, the parameters were as follows: echo time, 4.59 ms; repetition time, 22 ms; flip angle, 23°; RBW, 130 Hz/pixel; GRAPPA factor, 3; 32 reference lines.

### 1.2.2.3. Region growing

We used the raw input data format DICOM, which employs a TOF modality. Preprocessing procedures included anonymization using DICOM Anonymizer Pro (Neologica, Montenotte, Italy) and region growing by an in-house vessel analyzer program that created segmented brain angiography maps, converting them into the NII format. The internally developed vessel morphology pipelines then analyzed and extracted brain vessel features to examine the cerebrovascular structure. Figure 1 provides a schema of the intravascular feature vector extraction process. Intelligent morphological surface, centerline, bifurcation, and airway sectional processing algorithms were used to characterize vascular spots, segments, chunks, and branches. The procedures were finalized upon providing multifaceted systematic dimensions of the geometrically modeled features.

### 1.2.2.4. Feature extraction

To specify feature modeling, the dissection of isosurfaces for vessel surface model generation

was initially performed using the vascular modeling toolkit libraries.[6-9] The *z*-axis voxels were tailored to the isovoxel image scale using bicubic interpolation to minimize artifacts and rough image resampling on a regular planar grid.[10-12] A continuous 3D space was divided into myriad cells uniformly based on the respective vertices of their isosurfaces. The major arterial centerlines from the boundary surface of each cell were then extracted. At this stage, a set of spatial coordinates, whose nearest vertex among the vertices of the isosurface is homogeneously distributed, works as a unit cell. The framework determines the starting point and skeleton of the centerlines of the significant brain arteries from a lower slice of the vascular region for extraction. Vessel skeleton refinement strengthens the determination of the endpoints of the centerline. Specifically, (i) skeletonizing the cerebrovascular region and surface, (ii) pruning the branch under a predetermined threshold, (iii) generating a linked list of a tree structure based on the refined skeletal structure, and (iv) specifying leaf nodes from the linked list determine the endpoints. The centerlines were extracted by tracking the boundary surfaces of the cells connecting the start and end points. Finally, the pipelines characterized numerous blood vessel feature vectors of compartmentalized groups based on a branch point of a centerline. Quantified vessel characteristics include the cerebral blood vessel cross-sectional area, maximally inscribed sphere radius, minimized and maximized diameter, maximum-minimum radius ratio, surface circumference, distortion, curvature, and (hydraulic) luminal circularity (Table 1).

Thus, the vascular morphological modeling pipelines precede the preprocessing. This leads to surface extraction and re-meshing, centerline and branch extraction, and centerline merging to obtain its derivative subfeatures. The finalized vessel features then support ensemble neural networks to detect structural brain anomalies. The feature vectors accompany subject-wise gold-standard ground truth vascular labels established by two board-certified neurologists with expertise in stroke imaging and angiography.

### 1.2.3. Reframing hierarchical cerebrovasculature

In contrast to the conventional nomenclature employed in the clinical neurology field, approximately 4,000 detailed minuscule cerebral arterial segments, subdivided by our algorithm, required a dimensional reduction of the feature data for utilization in neurovascular research.

**Table 1. Evaluation method description of intracranial vasculature features.**

| Feature vectors | Evaluation |
|---|---|
| X, Y, and Z-coordinate | 3 dimensional cubic cell coordinate of X, Y, and Z axis in cartesian framework |
| Max inscribed sphere R | Insphere which is sphere contained within the vessel segment polyhedron tangent to surfaces of it |
| Hydraulic luminal diameter | Hydraulic diamter evaluated by ratio cross-sectional area of the flow to perimeter of the arterial segment channel |
| Minimum and maximum diameter | Maximum and minimum diameter calculated among the diameters within the vascular segment |
| Area | Cross sectional areas of vessel segment |
| Perimeter | Continuous line of boundary of geometric vessel channel |
| Luminal circularity | Roundness of lumen by $(4\pi*A)/P^2$ |
| Minimum to maximum diameter ratio | Ratio of maximized to minimized diameter calculated among the diameters within the vascular segment |
| Curvature | Degree of deviation of straight cylindric arterial channel |
| Torsion | Tortuosity parameter evaluated by path length, wavelength, and radius of curvature of an arterial segment |

*A*, area; *P*, perimeter

Therefore, we restructured the conventional concepts of the vascular unit system into four hierarchical levels (Figure 2). 'Spots' are the most rudimentary units of cubic cells in the binarised 3D cerebral arterial tree with an interval of 0.2801 mm on the arterial centerline. Each spot, along with its morphological features, was reorganized and hybridized into segments according to continuity and ending between bifurcations. According to the vessel geometry upon bifurcation, feature vector extraction algorithms geometrically grouped segments into 62 branches. Branches corresponded to the conventional cerebral arterial nomenclature. The vessel branches composed of the vascular segments could be reconstructed according to clinically practical criteria of symmetry: anterior or posterior, basal or pial, and MCA, ACA, or PCA. The cerebrovasculature consisted of 20 types of vessel chunks. The appropriateness of this system was validated using uniform manifold approximation and projection (UMAP).[13,14]

We provide a new nomenclature for the cerebral arteries (Table 2 and Table 3).

## 1.2.4. Classification method development

### 1.2.4.1. Two-step modeling

The primary objective of this study was the automatic segmentation and labeling of the cerebral vasculature using the conventional nomenclature (62 branches). To achieve this, we used a stepwise strategy: first allocating each spot of the whole brain to a specific chunk (step 1), and then allocating each spot of a single chunk to a specific branch (step 2). The supervised machine learning procedures initialized the allocation of each spot to a single chunk level using the multilayer perceptron neural network.[15-18] Input features included the coordinates of each spot, cerebral blood vessel cross-sectional area, maximally inscribed sphere radius, minimized and maximized diameter, maximum-minimum radius ratio, surface circumference, distortion, curvature, and (hydraulic) luminal circularity. Subsequently, the final chunk assignment was performed by allocating each spot to a specific chunk (step 1). A similar process was repeated to allocate spots in a specific chunk to a single branch by supervised machine learning, and the subsequent voting process enhanced accuracy (step 2). The voting algorithm obtained profiles of classified vessel labels from spots and selected the most frequently appearing vessel label among vascular chunks and segments.

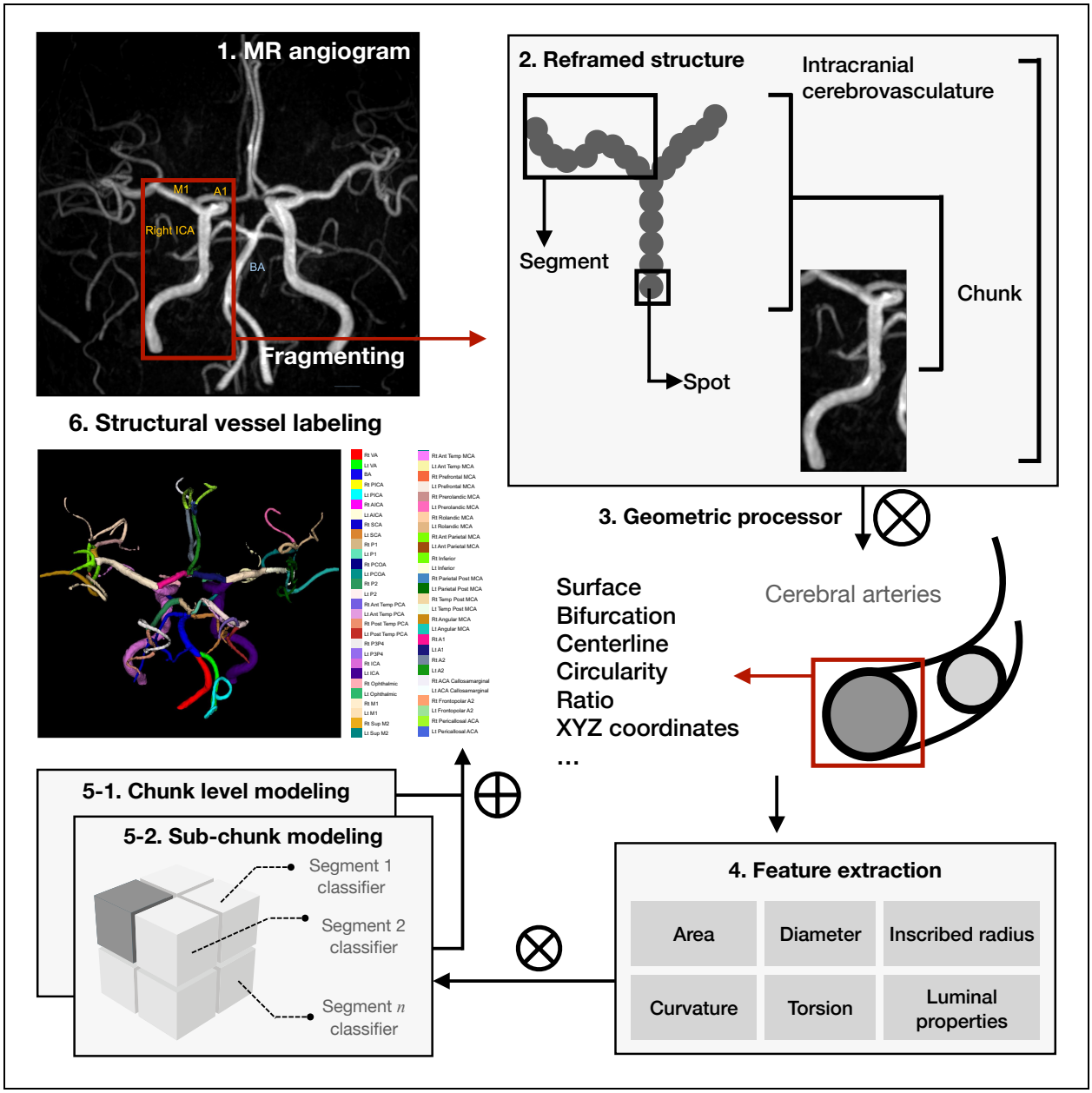


**Figure 2. Flow schema describes the comprehensive preprocessing procedures and the geometric characterization algorithms.**

Reconstruction encompasses vascular spots, segments, chunks, and branch units. Morphological and geometric characterization algorithms were used to process the vascular units automatically. A1, horizontal pre-communicating ACA; M1, sphenoidal middle cerebral artery; BA, basilar artery; ICA, internal carotid artery.

#### 1.2.4.2. Validation

An area under the receiver operating characteristic (AUROC) test was used to assess the internal and external validity and the chunk- and branch-level accuracy. First, we tested the performance of the algorithm in a set of independent stroke patients with ICAS. The structural dissimilarities in the cerebral arterial configuration between the healthy standard controls and those with stroke with ICAS were expected to indicate the clinical relevance of this algorithm in subjects with pathological conditions.

#### 1.2.4.3. Statistics

We performed groupwise $t$-statistics and ANOVA from the standpoints of feature vectors and vascular chunks to interpret between-group differences for statistical significance, details available in the results section. We visualized each group's similarity profiles in a two-dimensional plane, excluding $t$-values with $p$-values > 0.001 as insignificant.

#### 1.2.4.4. Data availability

According to the Korean governmental policy and health security policy of the data sharing committee of the Samsung Medical Center, all clinical information and brain image data are limitedly available through formal approval procedures upon requests to validated investigators. Further requests and inquiries are available to corresponding author (W.-K. Seo).

## 1.3. Results

### 1.3.1. Subject characteristics

Finally, we recruited 157 participants among the 203 screened subjects (42 / 50 controls, 46 / 77 stroke patients with ICAS, and 69 / 80 stroke patients; Figure 1).

**Table 2. Vessel branch compartmentalization into a 20-chunk macrovessel framework composed of 62 major arterial segments delineated the whole cohort-wise performance range of vessel chunks and segments.**

| Vessel chunk | Accuracy (%) | | | Precision (%) | | | Recall (%) | | | $F_1$ (%) | | |
|---|---|---|---|---|---|---|---|---|---|---|---|---|
| | Control | Stroke | ICAS | Control | Stroke | ICAS | Control | Stroke | ICAS | Control | Stroke | ICAS |
| Right ICA | 99 | 98 | 98 | 93 | 98 | 99 | 97 | 99 | 99 | 95 | 99 | 99 |
| Left ICA | 99 | 96 | 99 | 95 | 100 | 99 | 97 | 99 | 99 | 96 | 99 | 99 |
| Right anterior basal MCA | 95 | 90 | 92 | 84 | 96 | 95 | 82 | 97 | 96 | 83 | 97 | 96 |
| Left anterior basal MCA | 92 | 92 | 92 | 81 | 97 | 96 | 82 | 97 | 97 | 81 | 97 | 97 |
| Right anterior pial MCA | 98 | 96 | 99 | 97 | 99 | 99 | 97 | 99 | 100 | 97 | 99 | 99 |
| Left anterior pial MCA | 99 | 97 | 99 | 97 | 99 | 99 | 96 | 99 | 99 | 96 | 99 | 99 |
| Right anterior basal ACA | 91 | 87 | 89 | 72 | 95 | 96 | 68 | 95 | 94 | 70 | 95 | 95 |
| Left anterior basal ACA | 90 | 82 | 89 | 64 | 95 | 92 | 75 | 97 | 96 | 69 | 96 | 94 |
| Right anterior pial ACA | 91 | 90 | 95 | 70 | 95 | 97 | 66 | 96 | 96 | 68 | 96 | 96 |
| Left anterior pial ACA | 92 | 88 | 94 | 71 | 97 | 97 | 73 | 95 | 96 | 72 | 96 | 96 |
| Right posterior VA. | 97 | 95 | 96 | 79 | 94 | 96 | 75 | 97 | 96 | 77 | 96 | 96 |
| Left posterior VA. | 93 | 94 | 97 | 83 | 98 | 97 | 77 | 95 | 97 | 80 | 96 | 97 |
| Right posterior basal PCA | 97 | 91 | 97 | 80 | 97 | 98 | 84 | 98 | 97 | 82 | 97 | 97 |
| Left posterior basal PCA | 98 | 94 | 97 | 84 | 98 | 98 | 84 | 97 | 98 | 84 | 98 | 98 |
| Right posterior pial PCA | 87 | 87 | 93 | 69 | 97 | 97 | 65 | 86 | 96 | 67 | 91 | 96 |
| Left posterior pial PCA | 90 | 89 | 94 | 72 | 97 | 98 | 68 | 97 | 98 | 70 | 97 | 98 |
| Right SCA, AICA, and PICA | 96 | 94 | 95 | 84 | 93 | 96 | 90 | 98 | 98 | 87 | 96 | 97 |
| Left SCA, AICA, and PICA | 96 | 90 | 95 | 86 | 98 | 98 | 82 | 96 | 97 | 84 | 97 | 97 |
| BA | 96 | 93 | 95 | 85 | 97 | 96 | 80 | 97 | 95 | 82 | 97 | 96 |

[a]Each unit of major arterial segments was further condensed and tagged with identifiers composed of chunk and segment digits.
[b]Symmetrical properties of entire cerebrovascular branches were prefixed with ‘Right’ or ‘Left’; abbreviations are defined in the text.
[c]If the sample size was too small for inclusion in the test pool or there was only one type of branch within the chunk, the performance profile of the vessel branch was excluded.

**Table 3. Vessel branch compartmentalization into a 20-chunk macrovessel framework composed of 62 major arterial segments and delineated whole cohort-wise performance range of vessel chunks and segments.**

| Major arterial segment; vessel branch (serial) | Accuracy (%) | | | Precision (%) | | | Recall (%) | | | $F_1$ (%) | | |
|---|---|---|---|---|---|---|---|---|---|---|---|---|
| | Control | Stroke | ICAS | Control | Stroke | ICAS | Control | Stroke | ICAS | Control | Stroke | ICAS |
| Right ICA[b] (A1.01[a]) | 100 | 100 | 100 | 100 | 100 | 100 | 100 | 100 | 100 | 100 | 100 | 100 |
| Right OA (A1.02) | 97 | 92 | 98 | 97 | 95 | 95 | 95 | 98 | 98 | 96 | 97 | 97 |
| Left ICA (A2.01) | 100 | 100 | 100 | 100 | 100 | 100 | 100 | 100 | 100 | 100 | 100 | 100 |
| Left OA (A2.02) | 89 | 96 | 94 | 97 | 99 | 99 | 94 | 97 | 97 | 95 | 98 | 98 |
| Right M1 (A3.01) | 95 | 94 | 98 | 89 | 98 | 99 | 84 | 98 | 98 | 87 | 98 | 98 |
| Right MCAS (A3.02) | 88 | 91 | 96 | 70 | 97 | 95 | 79 | 96 | 95 | 74 | 96 | 95 |
| Right MCAI (A3.03) | 90 | 93 | 96 | 86 | 97 | 95 | 85 | 98 | 98 | 86 | 97 | 97 |
| Left M1 (A4.01) | 95 | 96 | 97 | 89 | 98 | 98 | 90 | 98 | 98 | 90 | 98 | 98 |
| Left MCAS (A4.02) | 88 | 89 | 95 | 74 | 95 | 93 | 80 | 97 | 95 | 77 | 96 | 94 |
| Left MCAI (A4.03) | 90 | 94 | 96 | 85 | 98 | 96 | 81 | 97 | 97 | 83 | 98 | 97 |
| Right MCALO (A7.01) | 87 | | 96 | | | 99 | | | 96 | | | 98 |
| Right MCAPR (A7.02) | 96 | 94 | 99 | 72 | 97 | 98 | 79 | 95 | 97 | 75 | 96 | 98 |
| Right MCAR (A7.03) | 93 | 96 | 95 | 68 | 96 | 96 | 74 | 97 | 98 | 71 | 97 | 97 |
| Right MCAAP (A7.04) | 92 | 91 | 95 | | 96 | 97 | | 95 | 97 | | 96 | 97 |
| Right MCAPP (A7.05) | 92 | 93 | 96 | | 96 | 97 | | 96 | 95 | | 96 | 96 |
| Right MCAA (A7.06) | 95 | 96 | 97 | 82 | 98 | 98 | 77 | 96 | 97 | 79 | 97 | 98 |
| Right MCAPT (A7.07) | 94 | 93 | 98 | 52 | 93 | 96 | 72 | 97 | 97 | 60 | 95 | 96 |
| Right MCAMT (A7.08) | 86 | 87 | 93 | | 97 | 92 | | 95 | 95 | | 96 | 94 |
| Right MCAAT (A7.09) | 73 | 94 | 89 | 70 | 96 | 87 | 74 | 96 | 94 | 72 | 96 | 90 |
| Left MCALO (A8.01) | 77 | | 92 | | | 95 | | | 88 | | | 91 |
| Left MCAPR (A8.02) | 95 | 96 | 98 | 67 | 96 | 98 | 71 | 95 | 99 | 69 | 95 | 98 |
| Left MCAR (A8.03) | 96 | 96 | 98 | 62 | 95 | 98 | 66 | 95 | 96 | 64 | 95 | 97 |
| Left MCAAP (A8.04) | 93 | 94 | 97 | 61 | 94 | 96 | 50 | 92 | 91 | 55 | 93 | 93 |
| Left MCAPP (A8.05) | 94 | 94 | 98 | 56 | 92 | 93 | 53 | 93 | 96 | 55 | 93 | 95 |
| Left MCAA (A8.06) | 95 | 97 | 98 | 85 | 97 | 98 | 79 | 97 | 97 | 82 | 97 | 98 |
| Left MCAPT (A8.07) | 94 | 95 | 97 | 57 | 93 | 94 | 67 | 95 | 97 | 61 | 94 | 95 |
| Left MCAMT (A8.08) | 84 | 92 | 92 | | 95 | 98 | | 94 | 99 | | 94 | 99 |
| Left MCAAT (A8.09) | 92 | 94 | 97 | 63 | 98 | 97 | 70 | 95 | 97 | 66 | 96 | 97 |
| Right A1A2 (A5.01) | | | | | | | | | | | | |
| Left A1A2 (A6.01) | | | | | | | | | | | | |
| Right ACAMO (A9.01) | 91 | 100 | 98 | | | 89 | | | 94 | | | 91 |
| Right A2F (A9.02) | 97 | 96 | 99 | 85 | 99 | 99 | 75 | 98 | 99 | 79 | 99 | 99 |
| Right ACAC (A9.03) | 97 | 94 | 99 | 81 | 98 | 99 | 89 | 99 | 99 | 85 | 99 | 99 |
| Right ACAP (A9.04) | 98 | 99 | 99 | 96 | 99 | 100 | 92 | 99 | 99 | 94 | 99 | 100 |
| Left ACAMO (A10.01) | 86 | | 95 | | | 96 | | | 91 | | | 93 |
| Left A2F (A10.02) | 91 | 93 | 96 | 77 | 94 | 98 | 69 | 98 | 98 | 73 | 96 | 98 |
| Left ACAC (A10.03) | 90 | 96 | 93 | 86 | 98 | 99 | 80 | 96 | 98 | 83 | 97 | 98 |
| Left ACAP (A10.04) | 98 | 98 | 99 | 90 | 98 | 99 | 95 | 99 | 99 | 93 | 98 | 99 |
| Right VA (P1.01) | | | | | | | | | | | | |
| Left VA (P2.01) | | | | | | | | | | | | |
| Right P1P2P3P4 (P3.01) | | | | | | | | | | | | |
| Left P1P2P3P4 (P4.01) | | | | | | | | | | | | |
| Right PCOA (P5.01) | 100 | 96 | 100 | 91 | 73 | 92 | 99 | 99 | 100 | 95 | 84 | 96 |
| Right HA[c] (P5.02) | | | | | | | | | | | | |

| | | | | | | | | | | | | |
|---|---|---|---|---|---|---|---|---|---|---|---|---|
| Right PCAAT (P5.03) | | | | | | | | | | | | |
| Right PCAPT (P5.04) | 99 | 99 | 100 | | | | | | | | | |
| Right PO (P5.05) | 89 | 93 | 95 | | | | | | | | | |
| Right PCALC (P5.06) | 97 | 96 | 99 | | | | | | | | | |
| Left PCOA (P6.01) | 97 | 94 | 99 | 98 | 100 | 100 | 97 | 95 | 96 | 98 | 97 | 98 |
| Left HA (P6.02) | | | | | | | | | | | | |
| Left PCAAT (P6.03) | 93 | 81 | 98 | 73 | 92 | 94 | 71 | 94 | 96 | 72 | 93 | 95 |
| Left PCAPT (P6.04) | 98 | 98 | 99 | 85 | 99 | 98 | 94 | 99 | 98 | 89 | 99 | 98 |
| Left PO (P6.05) | 94 | 96 | 98 | 70 | 98 | 99 | 57 | 97 | 98 | 63 | 98 | 98 |
| Left PCALC (P6.06) | 96 | 95 | 99 | 92 | 99 | 99 | 81 | 99 | 99 | 86 | 99 | 99 |
| Right PICA (P7.01) | 99 | 96 | 99 | 79 | 99 | 100 | 81 | 99 | 99 | 80 | 99 | 100 |
| Right AICA (P7.02) | 85 | 96 | 92 | 91 | 99 | 99 | 85 | 98 | 99 | 88 | 98 | 99 |
| Right SCA (P7.03) | 99 | 99 | 100 | 95 | 100 | 100 | 99 | 100 | 100 | 97 | 100 | 100 |
| Left PICA (P8.01) | 100 | 96 | 100 | 91 | 99 | 100 | 80 | 96 | 99 | 85 | 97 | 99 |
| Left AICA (P8.02) | 91 | 93 | 97 | 82 | 93 | 96 | 86 | 97 | 96 | 84 | 95 | 96 |
| Left SCA (P8.03) | 100 | 99 | 100 | 94 | 99 | 99 | 97 | 100 | 100 | 96 | 100 | 99 |
| BA (P0.00) | | | | | | | | | | | | |
| ACOA (A0.00) | | | | | | | | | | | | |

[a]Symmetrical properties of entire cerebrovascular branches were prefixed with ‘Right’ or ‘Left’; abbreviations are defined in the text.
[b]Each unit of major arterial segments was further condensed and tagged with identifiers composed of chunk and segment digits.
[c]If the sample size was too small for inclusion in the test pool or there was only one type of branch within the chunk, the performance profile of the vessel branch was excluded.

**Table 4. Demographic and clinical features of the cohorts (*n* = 157).**

| Cases | Control (*n* = 42) | Stroke with ICAS (*n* = 46) | Stroke (*n* = 69) | *p*-value[*] | *p*-value[†] | *p*-value[‡] |
|---|---|---|---|---|---|---|
| Sex, male | 31 (73.8) | 27 (58.7) | 77 (67.5) | 0.138 | <0.001 | 0.433 |
| Age, years | 58 ± 10.1 | 64.2 ± 13.3 | 69.3 ± 12.8 | 0.018 | <0.001 | <0.001 |
| Height, cm | 166.3 ± 8.3 | 161.5 ± 9.7 | 163.4 ± 9 | 0.016 | 0.923 | <0.001 |
| Weight, kg | 67.4 ± 10.9 | 63.7 ± 12.5 | 65.8 ± 11.4 | 0.148 | 0.637 | 0.008 |
| Hypertension | 16 (38.1) | 29 (63) | 74 (66.7) | 0.019 | 0.01 | <0.001 |
| Diabetes | 5 (11.9) | 18 (42.9) | 31 (27.9) | 0.003 | 0.877 | 0.003 |
| Hyperlipidemia | 11 (26.2) | 18 (42.9) | 56 (50.5) | 0.201 | 0.006 | <0.001 |
| Current smoking | 6 (16.7) | 11 (23.9) | 14 (20.3) | 0.671 | 0.067 | 0.162 |

[a]The intensity of smoking ranges from zero to two.
[b]The severity of alcohol ranges from zero to four.
[*]Boldened if $p < 0.05$. *P-values* statistically analyzed by homoscedastic two-sample t-test had two-tailed distribution parameters between the controls and stroke-with-ICAS patients.
[†]Homoscedastic two-sample t-test had two-tailed distribution parameters between the stroke-with-ICAS and stroke-only patients.
[‡]Homoscedastic two-sample t-test had two-tailed distribution parameters between the controls and stroke-only patients.
AF, atrial fibrillation

The training and test sets comprised 70% and 30%, respectively, of the healthy control group ($n$ = 42). The group had a mean age of 58 years (SD, 10.1 years; Table 4) and was predominantly male (73.8%). A stroke group was included to validate the algorithm. The same training–test ratio policy was used for the rest of the study cohorts. The stroke-with-ICAS group comprised 46 stroke patients (58.7% male), with a mean age of 64.2 years (SD, 13.3). No data were excluded for any of the variables used in the training or testing sets. Stroke patients were older and more likely to smoke cigarettes and have diabetes, hyperlipidemia, hypertension, or derivative coronary artery diseases than those in the control group.

### 1.3.2. Vascular component characteristics

Considering inter-subject hallmarks in the stepwise vessel identification process, the cerebrovascular images were evaluated under a vascular component profile containing 5016.4 ± 732.9 spots, 42.5 ± 4.2 segments, and 18.3 ± 0.8 chunks in controls; 4393.6 ± 1906.3 spots, 33.6 ± 11.7 segments, and 15.8 ± 4.3 chunks in patients with stroke with ICAS; and 4810.4 ± 1357.5 spots, 39 ± 7.6 segments, and 17.6 ± 1.9 chunks in patients with stroke. We considered the vessel unit distribution for each cohort to precisely analyze complex cerebral arterial trees (Figure 4).

We mapped the distribution profile of spots across the control, stroke-with-ICAS, and stroke groups (Figure 3). Regardless of study cohorts, concerning the vessel chunks, the most frequently appearing components were the right and left anterior pial MCA. They were followed by the right and left ICA, right anterior pial ACA, left posterior VA, and right and left posterior basal PCA with cohort-wise subtle fluctuations. Concerning the vessel segments, independent of the study groups, the four most frequently appearing vascular elements were the ICA and MCA angular branches, including the right and left branches. The following most frequent vascular segments included the pericallosal branch of the ACA and the posterior temporal branch of the PCA across the study groups, including the right and left branches.

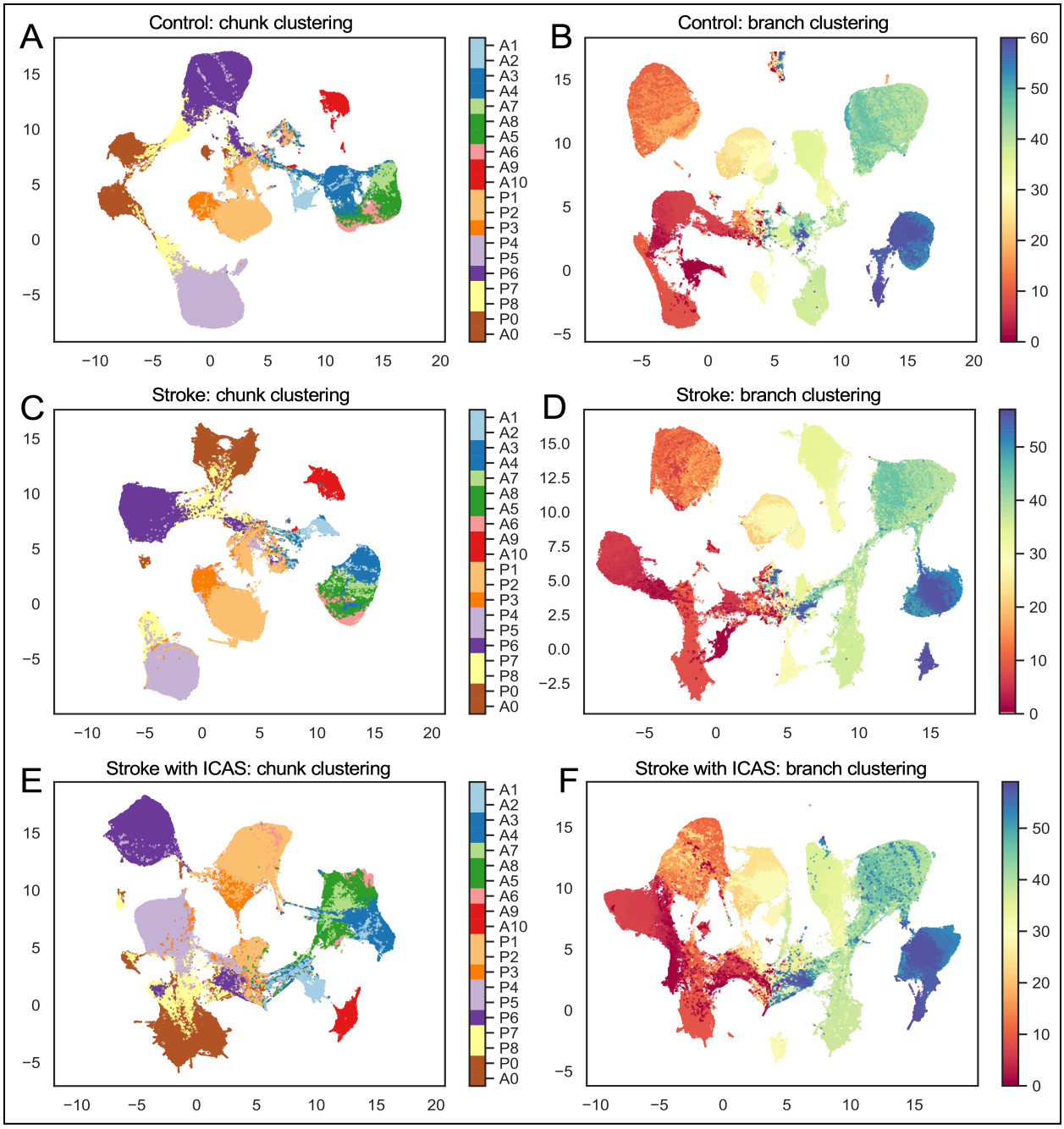


**Figure 3. Results of stochastic chunk- and segment-based cerebrovascular clustering analysis.**

Clustering mapping results are presented by (A) chunks in the control group, (B) segments in the control group, (C) chunks in the ICAS group, (D) segments in the ICAS group, (E) chunks in TOAST levels 1–3, (F) segments in TOAST levels 1–3, (G) chunks in the stroke group, and (H) segments in the stroke group.

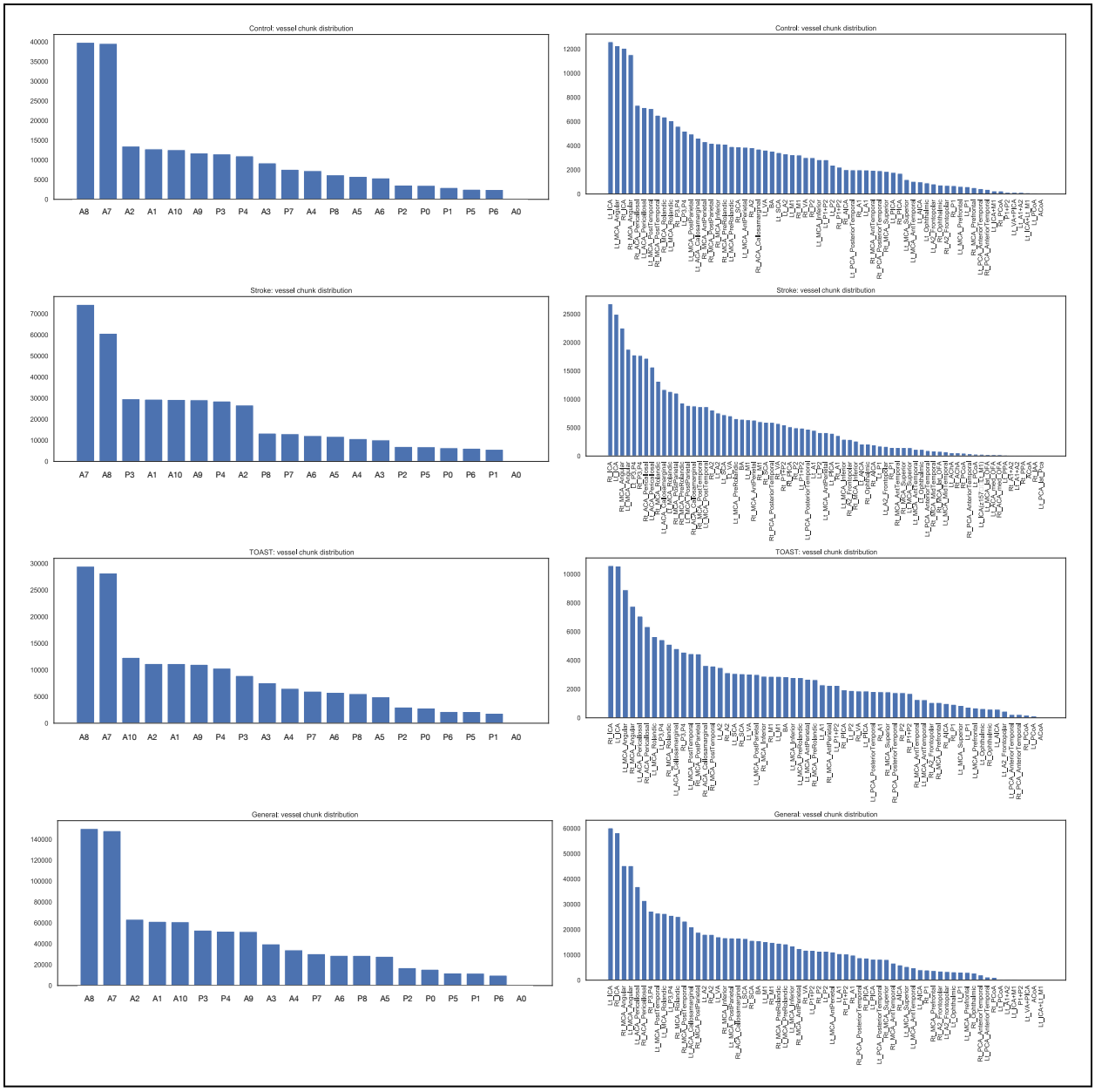


**Figure 4. Cohort-wise vessel count profiles scaled in vascular chunk and segment.**

The results show the distribution of vessel components scaled in chunks and segments investigating dominant vessel components in each cohort.

### 1.3.3. Testing the appropriateness of the reframed vascular structure

We evaluated the appropriateness of the reframed vascular elements by unsupervised dimensional reduction using the UMAP and visualized the cluster results in the planar space with color mapping according to the 20 types of vessel chunks (Figure 3-A, C, and E). The dimensionality reduction had nonlinear properties, and the global data structure was conserved. Each chunk's lesional profile precisely depicted the characteristics of each vessel, and the embedding algorithms efficiently captured high dimensions. The qualitative observations showed that the control, stroke, and stroke-with-ICAS groups had similar overall accuracy in clustering.

Figures 4-B, D, and F depict the unsupervised clustering of the spots visualizing each conventional vascular branch. Unlike in the chunk-level mapping, the branch-level clustering was insufficient to discriminate each branch.

### 1.3.4. Step 1 modeling: chunk

The model ensemble identified 20 chunks with 87–99% accuracy (Figure 5), except in the left anterior basal ACA chunk in the stroke group (82%). The anterior communicating artery (ACOA; A0) showed cohort-wise fluctuating performance attributable to sample size constraints and significant anatomical variations (37–91%). The training and test sets included both epitomized and anomalous (Figure 5A) 3D vascular component coordinates and derivative features at each spot vector as inputs. The controls, stroke cohort, and stroke-with-ICAS cohort gave similar results in that, except for A0, most of the vessel chunks (between 90–99%) were successfully classifiable. In the chunk prediction results of the control group (Figure 5B), the majority of chunks showed 90–99% accuracy, except for the A0 (0.36) and P5 chunks (pial branches of the right posterior cerebral artery; 0.87). In the stroke group, only A5, A6, A10, P5, and P6 (basal branches of the right and left anterior cerebral artery, pial branches of the left anterior cerebral artery, and pial branches of the right and left posterior cerebral artery; 0.82–0.89) with A0 (0.37) fell outside the 90–99% range (Figure 5D). In patients with ICAS (Figure 5C), A5 and A6 (basal branches of the right and left anterior cerebral artery; 0.89) had an 89% accuracy and the rest of the branches, excluding ACOA, ranged within a 91–99% precision.

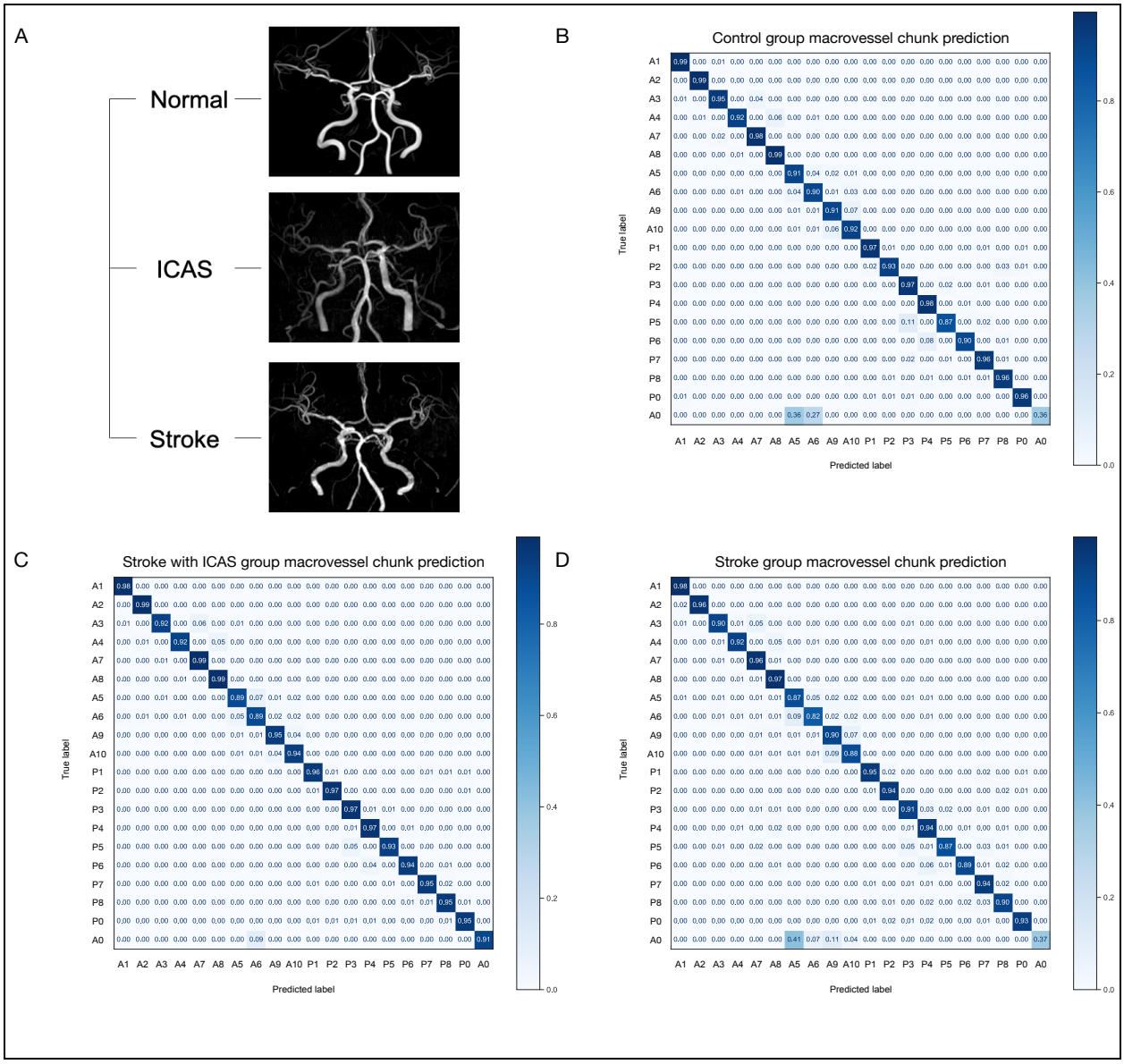


**Figure 5. Prediction performance profiles of a 20-chunk macrovessel in the control, ICAS, and stroke group cohorts.**

(A) Examples of 3D cerebrovascular models of the disease-free healthy subjects, stroke-only patients, and stroke-with-ICAS patients. Macrovessel chunk prediction results of (B) control cohorts, (C) ICAS cohorts, and (D) stroke cohorts are shown.

When training both controls and stroke patients as a general group in chunk predictions (Figure 5D), except for ACOA, the right and left anterior basal ACA and right and left posterior pial PCA chunks had an 82–89% performance. The rest showed unexceptional performances (90–98%) before the post-processing procedures.

With regard to sensitivity and specificity, the area under the curve (AUC) of the receiver operating characteristic (ROC) curve showed an overall value of 0.99–1.00 (0.97–1.00), and the precision-recall curve (PRC) was 0.992 (0.626–0.999) for the control, ICAS, and stroke cohorts. The algorithm's AUC accuracy improved from 0.56–0.96 (95% CI 0.52–0.96; Table 5) to 0.62–0.98 (95% CI 0.56–0.98; Table 5) after applying the voting procedure, with statistical significance ($p < 0.001$) observed in all cases except for A5 and P5.

### 1.3.5. Step 2 modeling: branch

With regard to the branch-level classification of 62 branches in the controls, each spot had the following accuracy, except for a few exceptions: A1-A2: 89–100%, A3–A8: 73-96%, A9–A10: 86–98%, P5-P6: 89–100%, and P7-P8: 85–100% (Figure 6, Table 2, and Table 3). The control results showed that, except for A2.02, A3.02, A4.02, A7.01, A7.08, A7.09, A8.01, A8.08, A10.01, P5.05, and P7.02, the overall classification performance was roughly 90–99% (Table 2 and Table 3). In the analysis of classification performance in the stroke cohorts, the following precision capacities were observed: A1-A2: 92–100%, A3-A8: 87–97%, A9-A10: 93–100%, P5-P6: 81–99%, and P7-P8: 93–99% (Figure 6, Table 2, and Table 3). Considering the deviations in the classification performance of the A4.02, A7.08, and P6.03 segments in the stroke group, the categorization performance showed percentage values in the upper 90s (Table 2 and Table 3). Further details of the classification performance are presented in Table 2 and Table 3. For segment-wise categorization in ICAS patients, each type of segment had the following performance: A1-A2: 94–100%, A3-A8: 89–99%, A9-A10: 93–99%, P5-P6: 95–100%, and P7-P8: 92–100% (Figure 6, Table 2 and, Table 3). Except for segment A7.09, the overall accuracy profile rarely fell below 90% (Table 2 and Table 3).

Concerning sensitivity and specificity, the AUC-ROC showed an overall value of 0.99 (0.97–1.00), and the PRC was 0.992 (0.483–0.975) for the control, ICAS, and stroke cohorts scaled to macro-average and micro-average values (Figure 8).

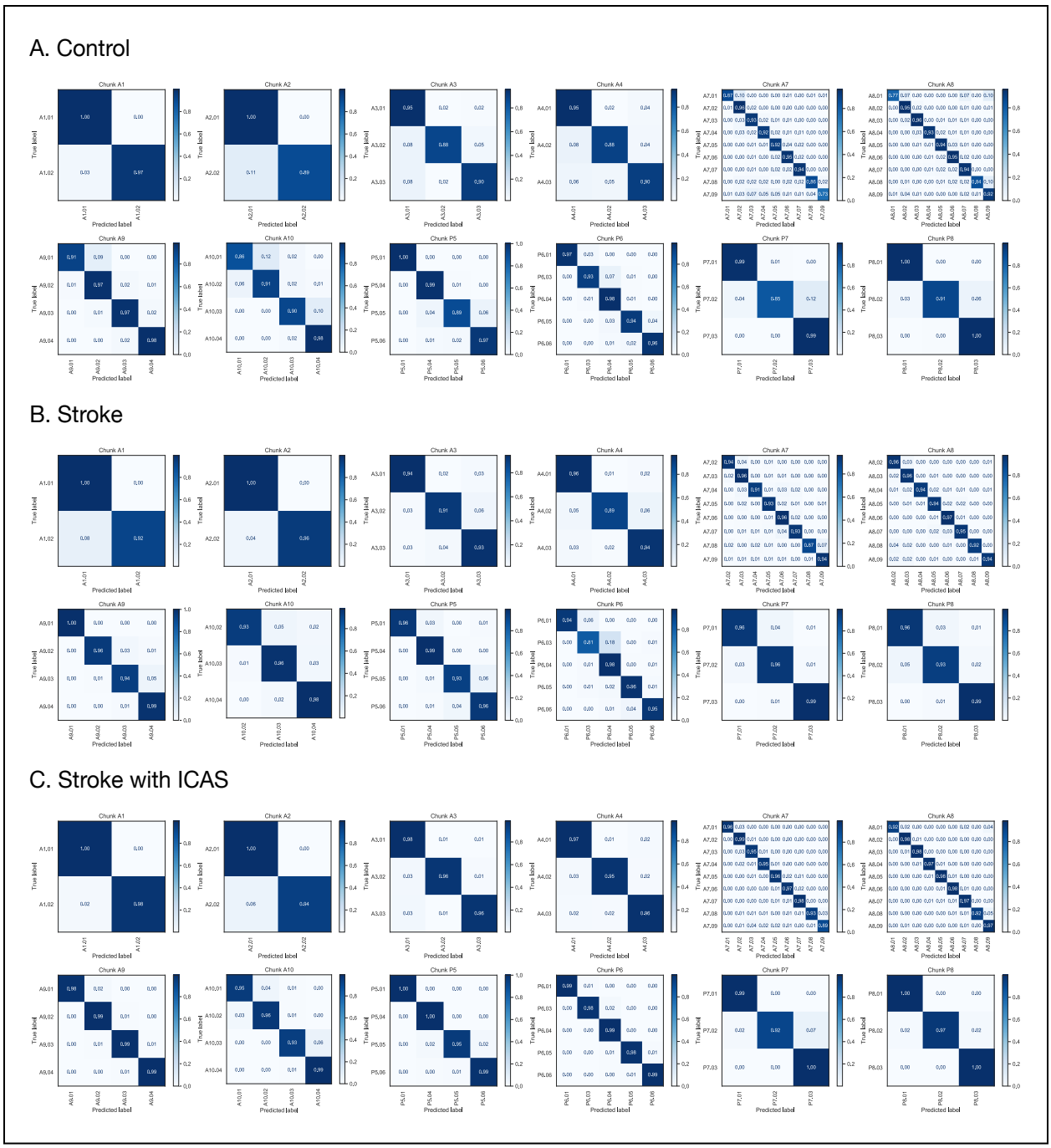


**Figure 6. Prediction performance profiles of 62 major arterial branches in control, stroke-with-ICAS, and stroke group cohorts.**

The right and left posterior VA, BA, and ACOA chunks only include one significant type of arterial segment. The (A) control, (B) stroke, and (C) stroke-with-ICAS groups showed significant arterial segment classification capacity in the A0–A10 and P0–P8 chunks.

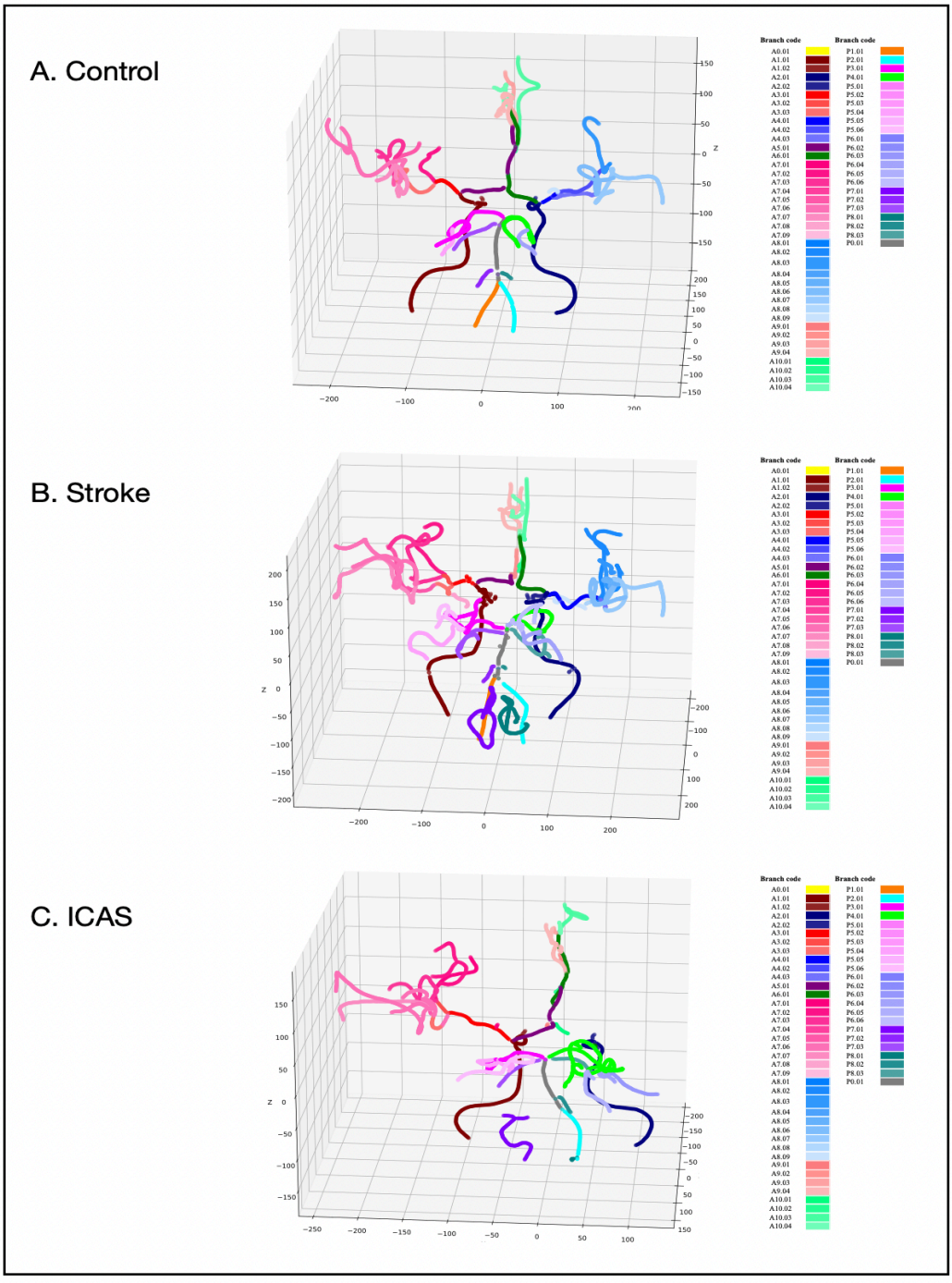


**Figure 7. Clinical cases of the control, stroke, and ICAS groups compared with predictively modeled vessel labels.**

Controls, stroke patients, and stroke-with-ICAS patients underwent color labeling and visualization according to the branch within the cerebrovasculature. The algorithm consistently showed good performance for cerebral arterial branch identification among healthy controls, stroke patients, and stroke patients with ICAS. The structural abnormalities in patients with ICAS produced no significant adverse effects on identification performance.

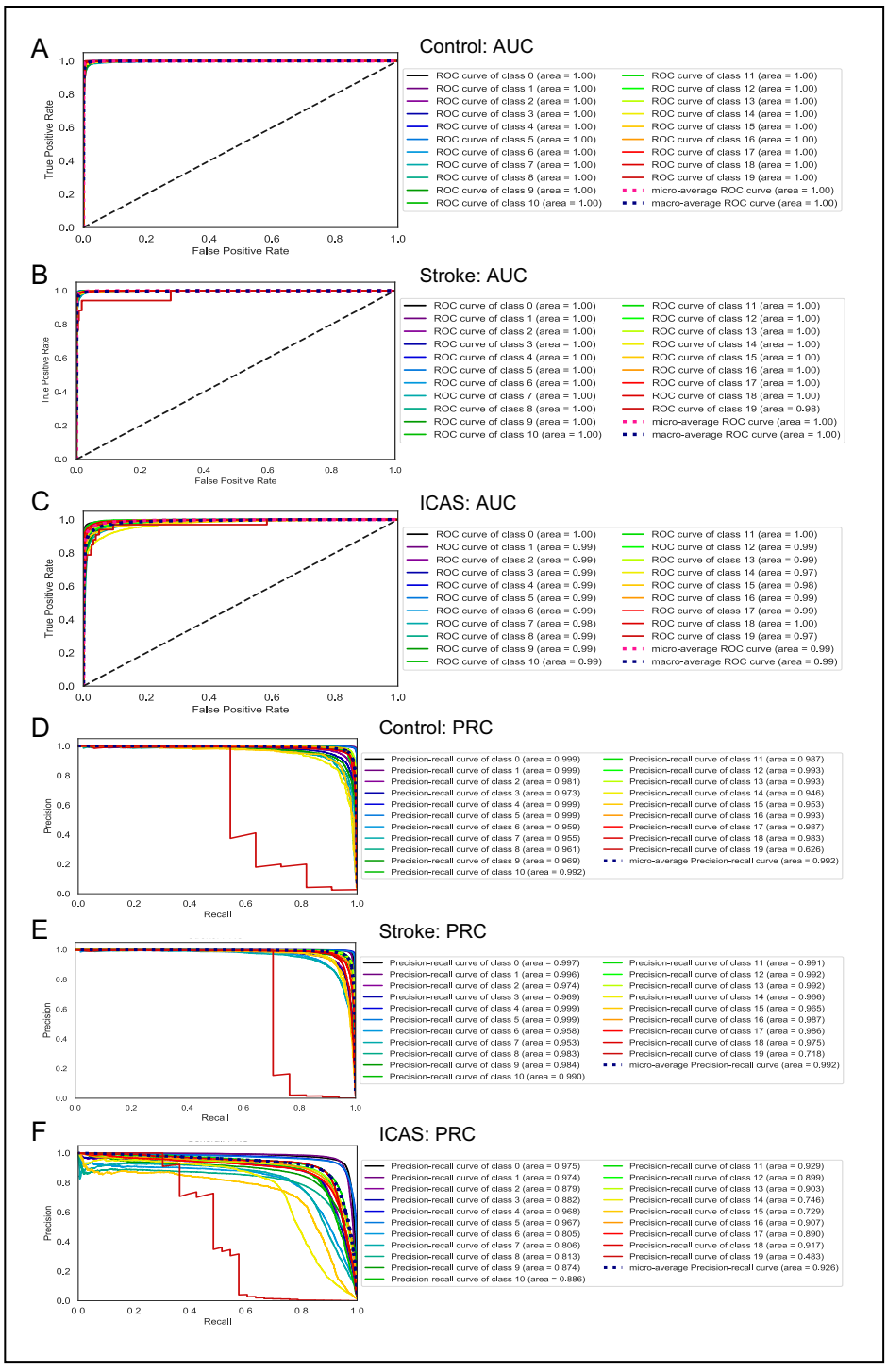


**Figure 8. Cohort-wise receiver operating characteristic and precision-recall curve scaled in vessel chunk.**

The results show the receiver operating characteristic and precision-recall curves of vessel components scaled in chunks investigating classification performance validation in each cohort. (A/D), (B/E), and (C/F) figures refer to area under receiver operation characteristic curve (AUC) and precision-recall curve (PRC) in disease free healthy subjects, stroke patients, and stroke-with-ICAS patients.

**Table 5. Comparison of the chunk-level discrimination performance between the models with and without the voting procedure.**

| Chunk | | Without voting | With voting | *p*-value |
|---|---|---|---|---|
| Number | Name | AUC (95% CI) | AUC (95% CI) | |
| A0 | ACOA | 0.56 (0.52 - 0.60) | 0.62 (0.56 - 0.67) | 0.015 |
| A1 | Right ICA | 0.90 (0.90 - 0.91) | 0.94 (0.94 - 0.94) | <0.001 |
| A2 | Left ICA | 0.92 (0.92 - 0.92) | 0.96 (0.95 - 0.96) | <0.001 |
| A3 | Right anterior basal MCA | 0.81 (0.81 - 0.82) | 0.85 (0.84 - 0.86) | <0.001 |
| A4 | Left anterior basal MCA | 0.81 (0.80 - 0.81) | 0.85 (0.85 - 0.86) | <0.001 |
| A7 | Right anterior pial MCA | 0.69 (0.69 - 0.70) | 0.70 (0.69 - 0.70) | 0.644 |
| A8 | Left anterior pial MCA | 0.72 (0.71 - 0.72) | 0.75 (0.75 - 0.76) | <0.001 |
| A5 | Right anterior basal ACA | 0.95 (0.95 - 0.95) | 0.97 (0.97 - 0.97) | <0.001 |
| A6 | Left anterior basal ACA | 0.96 (0.96 - 0.96) | 0.98 (0.98 - 0.98) | <0.001 |
| A9 | Right anterior pial ACA | 0.73 (0.73 - 0.74) | 0.76 (0.76 - 0.77) | <0.001 |
| A10 | Left anterior pial ACA | 0.75 (0.74 - 0.75) | 0.77 (0.77 - 0.78) | <0.001 |
| P1 | Right posterior VA | 0.81 (0.80 - 0.81) | 0.85 (0.84 - 0.85) | <0.001 |
| P2 | Left posterior VA | 0.81 (0.80 - 0.82) | 0.84 (0.83 - 0.85) | <0.001 |
| P3 | Right posterior basal PCA | 0.81 (0.81 - 0.82) | 0.83 (0.83 - 0.84) | <0.001 |
| P4 | Left posterior basal PCA | 0.86 (0.86 - 0.86) | 0.90 (0.90 - 0.91) | <0.001 |
| P5 | Right posterior pial PCA | 0.90 (0.89 - 0.90) | 0.95 (0.94 - 0.95) | <0.001 |
| P6 | Left posterior pial PCA | 0.70 (0.68 - 0.71) | 0.71 (0.70 - 0.72) | 0.064 |
| P7 | Right SCA, AICA, and PICA | 0.73 (0.72 - 0.75) | 0.71 (0.70 - 0.72) | <0.001 |
| P8 | Left SCA, AICA, and PICA | 0.86 (0.86 - 0.87) | 0.90 (0.89 - 0.90) | <0.001 |
| P0 | BA | 0.80 (0.80 - 0.81) | 0.86 (0.86 - 0.87) | <0.001 |

Excluding the voting area under the curve (AUC) allows for each spot to be allocated correctly into a specific chunk using only the multi-layer perceptron (MLP) neural network. In contrast, AUC with voting allows for the same possibility using a hybridized model composed of the MLP neural network and a voting procedure. ROC curve analysis comparing voting and non-voting was performed.

### 1.3.6. Vascular morphological features according to the vascular risk factors

Figure 9 presents differences in vascular morphological features among the control, stroke, and stroke-with-ICAS groups at each chunk. Notably, the phenomenon was conspicuous in the right ICA, left ICA, right anterior pial, and left anterior pial MCA chunks (Figure 7). The ICAS group had similar propensities concerning characterized geometric features. However, we also discovered the following unforeseen heterogeneous chunks between the control-stroke-ICAS functional profiles (Figure 7): anterior basal MCA, right anterior basal ACA, left anterior basal, right anterior pial ACA, and left anterior pial ACA.

### 1.3.7. The profiles of geometric feature vectors weighted on deep neural networks

The sensitivity and specificity results summarised by the AUROC revealed an overall micro-average performance of 0.97 and macro-average performance of 0.96 (Figure 10A and Figure 11) to discern stroke patients ($n$ = 40) as external validation subjects, employing healthy subjects as the training set. When externally validated by the stroke-with-ICAS group ($n$ = 46), the micro-average and macro-average performance values were 0.95 and 0.92, respectively (Figure 10B and Figure 11). For the external stroke patients, the AUROC performance ranged beyond the threshold of 0.95 for the entire vascular chunks except for A0, A5-6, A9, and P1-2, which spanned the 0.91–0.94 range. In contrast, in the external stroke-with-ICAS group, the AUROC scores of the vessel chunks A2, A4, A7-8, P2, and P7-8 exhibited values more extraordinary than the 0.95 capacity, leaving the rest of the chunks to bear performances between 0.90 and 0.94 (except for chunk A6 [0.89] and chunk A0 [0.70]).

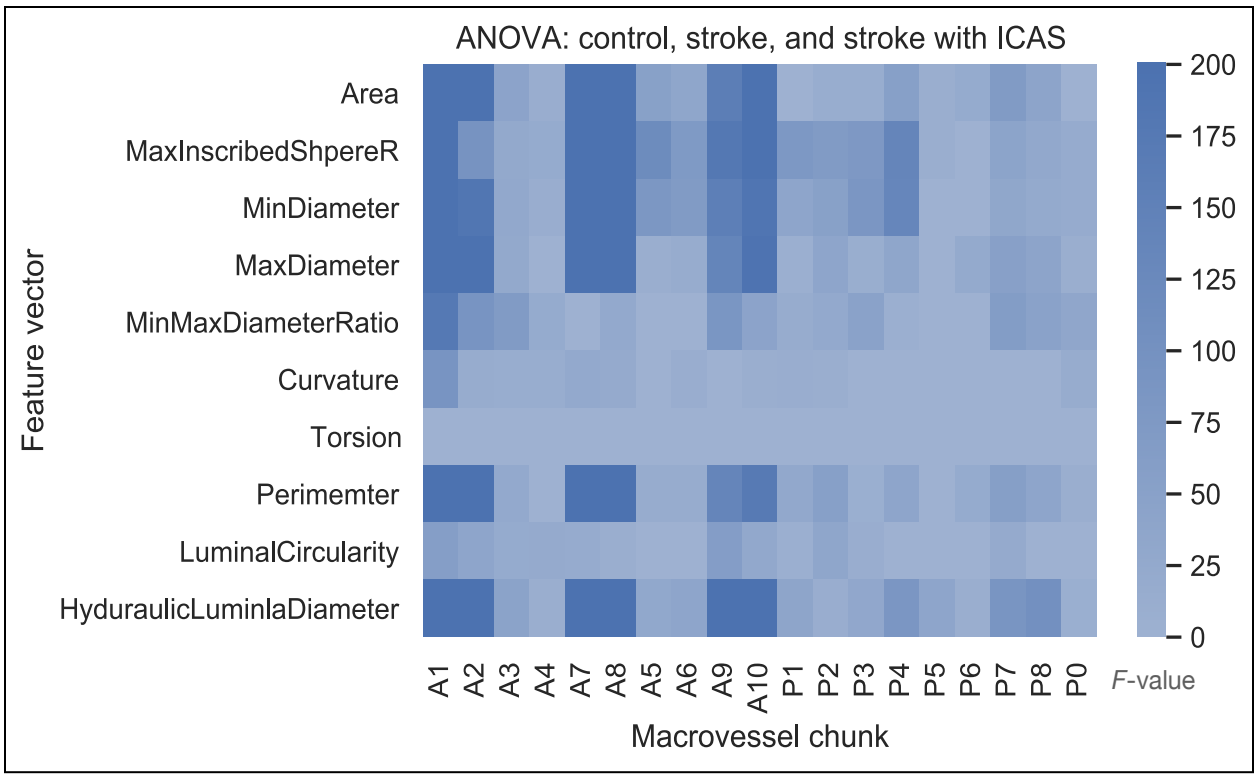


**Figure 9. Results of ANOVA F-statistics with analysis of the vascular characterization vectors and macrovascular chunks.**

The ANOVA values with p-values greater than 0.001 were considered insignificant and marginalized as zero. The results of the ANOVA compare the control, stroke, and stroke-with-ICAS groups.

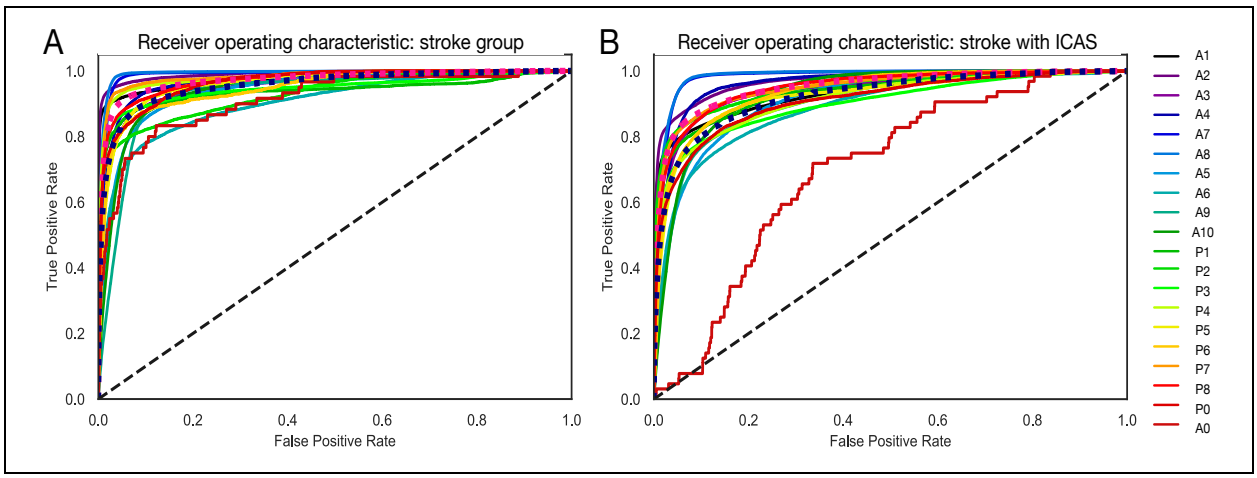


**Figure 10. External validation via the receiver operating characteristic in the stroke-only and stroke-with-ICAS groups.**

We analyzed the area under the receiver operating characteristic curve for the external validation of each spot's deep neural network ensemble to a specific chunk for stroke patients. The employed model ensemble received training only with a control group tested and validated by (A) the stroke group and (B) the stroke-with-ICAS group.

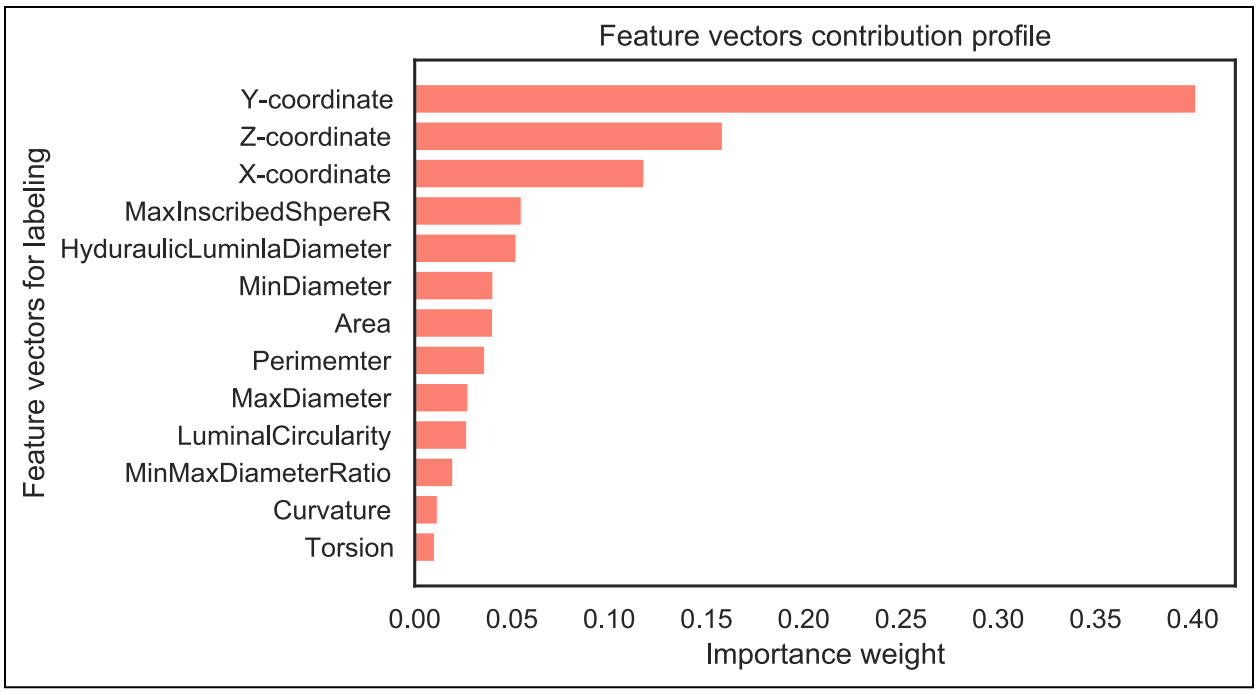


**Figure 11. The contribution profiles of geometric feature vectors weighted when training and employing deep neural networks.**

The contribution of Cartesian coordinates and geometric features when using the model ensemble trained only by a control group tested and validated by a stroke-with-ICAS group with a hierarchy.

## 1.4. Discussion

This study demonstrated that patient-specific cerebral arterial profiles aid in the quantitative and in-depth labeling of cerebral arterial branches that is clinically useful.[19-24] We hypothesized that: (i) the appropriate combination of classical anatomical rules and computational prediction expedites the exhaustive classification of cerebral arteries; (ii) variations in vessel branches are detectable by employing neural networks. Accordingly, we designed a deep-learning algorithm that intelligently established in-depth vascular territories using strategies stemming from the systematic geometric characterization of MRA data. The preprocessing modules uniquely reframed the entire cerebrovasculature into clinically redefined compartments: spots, segments, chunks, and branches.

A quantitative approach to investigating cerebrovasculature has shown limited success, and conventional approaches have used less precise quantitative methods to understand complex cerebrovascular structures with limited clinical relevance.[25-27] In previous attempts, vascular structures were overlooked, and distortion during thresholding was not adequately accounted for due to the shortage of appropriate geometric characterization algorithms for examining small vessels. Additionally, these methods inadequately assessed residual variation, leading to overfitting, and thus their conclusions must be considered with caution. Furthermore, the cerebrovascular coverage of previous studies is lacking,[27-29] even excluding some vessel categories that were too complex to classify. The arterial geometry has also not been characterized; they are, therefore, vulnerable to normal variations.

MRA is one of the most widely used tools for assessing cerebral arterial disease. Using its template alignment, attempts have been made to label cerebral arteries limited to variations of those underlying the anterior circulation and those in clinical datasets or by bifurcations of interest, covering only roughly eight territorial frameworks using typical angiography of healthy subjects.[2,30-33] Therefore, we cannot claim to have included all of the components of the cerebrovasculature in our analysis. Several graph neural network studies have facilitated the construction of arterial morphometry, assuming that arterial traces are entirely intact and typically representative. In other words, their hypotheses are vulnerable to interpreting vascular abnormalities or variations such as vessel occlusion.[3,25,26,34-36] Thus, conventional anatomical rules are less appropriate for quantitatively understanding the cerebrovasculature.

### 1.4.1. The role of neural networks in this study

The deep neural networks employed 3D coordinates and geometric vessel feature vectors (Figure 7) derived from the reframed vascular fragments. We specifically tagged them into major arterial branches by employing segment-wise voting algorithms and orchestrated neural networks, creating 62 intelligently identifiable vessel territories. Implementing these algorithms does not require heavy graphics microprocessors, high resolution, advanced noise nullification, or a specific region of interest choice.

By stochastically clustering the classified vascular regions, we identified blood vessels by exploiting the conventional neuroanatomical branch nomenclature. Finally, we propose that morphological parameters such as diameter, roundness, and tortuosity strengthen characterization vectors complementing variations under the Cartesian coordinates of angiographical categories. Therefore, reduced dependence on a Cartesian framework, owing to an overall uniform distribution of the contribution of geometric vascular features, lends this study a high level of robustness and reliability of performance.

Cerebral arterial labeling is not only a function of accuracy; therefore, targeted vessel chunks and segment ranges of the ensemble classifier cover should be exhaustive to fulfil clinical potential. Usually, pathological variations in the cerebral vasculature are expected to lower labeling performance. However, the multifaceted structural analysis among healthy controls, stroke patients, and stroke patients with ICAS revealed only a trivial difference in the performance of identifying each cerebral arterial branch (Figure 7). Considering the consistent labeling performance of this algorithm, the distinct contribution of the weighting algorithm of each cubic cell consisting of a 3D vessel model is worthy of continued focus in future studies to improve accuracy. The prestructured models require an entire cerebral arterial label identification time of no more than a minute, unbridled by manual visual inspection bias and observer variabilities.[37-39] Therefore, this algorithm can be applied to investigate cerebrovascular morphological features in various settings, such as in a longitudinal study, assessment of drug effects, and between-group comparison.

### 1.4.2. Paradigm-shifting vascular unit reframing

A mainstream strength of this study is the vascular framing using ‘chunk’, a critical element

referring to a group of cerebrovascular elements sharing functional and anatomical similarities. As substantiated by the comparative analysis of UMAP assessment group-wise chunk-level feature vectors, chunk-level analysis is a rational categorization method for territorializing cerebrovascular regions. Chunk discernment is a salient approach in a fundamental unit framework dedicated to the quantitative analysis of the cerebrovasculature and as an intermediate stage of vessel classification. Furthermore, this reframing reduces data dimension from about 5,000 spots to 20 chunks level, providing a valuable way of analyzing and summarising the massive data into a valid format.

### 1.4.3. Limitations and future directions

Several limitations exist. First, the results of this study have a limitation of generalizability. This study included participants with only an ischemic stroke rather than a hemorrhagic stroke. Thus, there are some potential challenges in discerning the various subtypes of the stroke to improve further the feasibility of the clinical application of neural network ensembles. In addition, all subjects were ethnically Korean. Considering the anatomical and pathological inter-racial differences in the intracranial cerebral vasculature, the performance of the model should be validated in different populations. Bespeaking generalizability and inter-institutional compatibility require additional external validation using images outside the Samsung Medical Center. Second, we acknowledge that the sample size at present is not sufficiently large; however, based on patient-specific profiles, we have provided the potential for finding additional novel brain frailty biomarkers. Third, our results indicate that neural networks effectively identify the cerebral arterial segment. However, a few structure-ambiguous vascular segments suffer from unsatisfactory performance complemented via segment-wise voting post-processing. We hypothesize that the enigmatic nature of some small vessel segments predisposes them to idiosyncratic performances. The geometric features of the developed redefined vascular units provide groundbreaking opportunities to interpret mixed vascular territories intelligently. However, covering various subjects with reproducible iterative measurements and theorizing optimized feature combinations remains an important scientific question. Another limitation of this study is that we only used TOF MR angiographic images. MRA does not, per se, provide authentic structural images but includes hemodynamic information. Therefore, modifications are mandatory if we apply the model developed in this study to other imaging modalities, such as digital subtraction angiography or computed

tomographic angiography.

A strength of this study lies in the unconventional accuracy of in-depth labeling that can outperform board-certified experts. Our system utilizes segment-wise voting algorithms, anatomical post-processing, paradigm-shifting vascular unit reframing, and robust systematic geometric feature characterization for clinical usability. The model performance was further synchronized and engineered using anatomical rule-assisted post-processing complementation. Exhaustive categorization resulted in segmenting the 20 vascular chunks, which were narrowed down and further classified into small vessel segment compartments composed of spot cells. The unlimited applicability of orchestrated neural networks to non-matched feature vector data provides patient-specific profiles, facilitating successful clinical interpretations, the potential prognosis of brain debility progression, and post-stroke treatment management.

## 1.5. Conclusions

In conclusion, we have pioneered the in-depth labeling cerebral arterial segments by scrutinizing neural network ensembles via cerebrovascular structural reframing. By systematically analyzing diverse cohorts, our results demonstrate that this technique is feasible and robust in profiling vessel-specific labeling.

## 1.6. Acknowledgements

The authors are thankful for the constructive statistical feature modeling guidance from the Medical Image Processing Lab, Sungkyunkwan University, and thank the study participants for their generous assistance with our research.

## 1.7. Funding

The study received support for the research project “Development of integrated brain-vascular imaging database for brain and cerebrovascular disease” (ID: NRF-2020M3E5D2A01084891) from the National Research Foundation of Korea (NRF) research grants.

# Bibliography


1. Dunas T, Wahlin A, Ambarki K, et al. Automatic labeling of cerebral arteries in magnetic resonance angiography. *MAGMA*. Feb 2016;29(1):39-47. doi:10.1007/s10334-015-0512-5

2. Dunas T, Wahlin A, Ambarki K, Zarrinkoob L, Malm J, Eklund A. A stereotactic probabilistic atlas for the major cerebral arteries. *Neuroinformatics*. Jan 2017;15(1):101-110. doi:10.1007/s12021-016-9320-y

3. Chen L, Hatsukami T, Hwang J-N, Yuan C. Automated intracranial artery labeling using a graph neural network and hierarchical refinement. Springer; 2020:76-85.

4. Alpers BJ, Berry RG. Circle of Willis in cerebral vascular disorders. The anatomical structure. *Arch Neurol*. Apr 1963;8:398-402. doi:10.1001/archneur.1963.00460040068006

5. Chung JW, Cha J, Lee MJ, et al. Intensive statin treatment in acute ischaemic stroke patients with intracranial atherosclerosis: a high-resolution magnetic resonance imaging study (STAMINA-MRI study). *J Neurol Neurosurg Psychiatry*. Feb 2020;91(2):204-211. doi:10.1136/jnnp-2019-320893

6. Piccinelli M, Veneziani A, Steinman DA, Remuzzi A, Antiga L. A framework for geometric analysis of vascular structures: application to cerebral aneurysms. *IEEE Trans Med Imaging*. Aug 2009;28(8):1141-55. doi:10.1109/TMI.2009.2021652

7. Izzo R, Steinman D, Manini S, Antiga L. The vascular modeling toolkit: a Python library for the analysis of tubular structures in medical images. *Journal of Open Source Software*. 2018;3(25):745.

8. Volkau I, Zheng W, Baimouratov R, Aziz A, Nowinski WL. Geometric modeling of the human normal cerebral arterial system. *IEEE transactions on medical imaging*. 2005;24(4):529-539.

9. Bühler K, Felkel P, La Cruz A. Geometric methods for vessel visualization and quantification—a survey. *Geometric modeling for scientific visualization*. 2004:399-419.

10. Keys R. Cubic convolution interpolation for digital image processing. *IEEE transactions on acoustics, speech, and signal processing*. 1981;29(6):1153-1160.

11. Rifman SS. Digital rectification of ERTS multispectral imagery. 1973:1131-1142.

12. Bernstein R. Digital image processing of earth observation sensor data. *IBM Journal of research and development*. 1976;20(1):40-57.

13. McInnes L, Healy J, Melville J. UMAP: Uniform manifold approximation and projection for dimension reduction. *arXiv preprint arXiv:180203426*. 2018;

14. Becht E, McInnes L, Healy J, et al. Dimensionality reduction for visualizing single-cell data using UMAP. *Nature Biotechnology*. 2019;37(1):38-44.

15. Hinton GE. Connectionist learning procedures. *Mach Learn*. Elsevier; 1990:555-610.

16. Glorot X, Bengio Y. Understanding the difficulty of training deep feedforward neural networks. presented at: Proceedings of the 30th international conference on artificial intelligence and statistics; 2010;

17. He K, Zhang X, Ren S, Sun J. Delving deep into rectifiers: surpassing human-level performance on imagenet classification. Proc IEEE Int Conf Comput Vis; 2015:1026-1034.

18. Kingma DP, Ba J. Adam: a method for stochastic optimization. *arXiv preprint arXiv:14126980*. 2014;
19. Chng SM, Petersen ET, Zimine I, Sitoh YY, Lim CC, Golay X. Territorial arterial spin labeling in the assessment of collateral circulation: comparison with digital subtraction angiography. *Stroke*. Dec 2008;39(12):3248-54. doi:10.1161/STROKEAHA.108.520593
20. Kitajima M, Hirai T, Shigematsu Y, et al. Assessment of cerebral perfusion from bypass arteries using magnetic resonance regional perfusion imaging in patients with moyamoya disease. *Jpn J Radiol*. Dec 2010;28(10):746-53. doi:10.1007/s11604-010-0507-0
21. Yan L, Salamon N, Wang DJ. Time-resolved noncontrast enhanced 4-D dynamic magnetic resonance angiography using multibolus TrueFISP-based spin tagging with alternating radiofrequency (TrueSTAR). *Magn Reson Med*. Feb 2014;71(2):551-60. doi:10.1002/mrm.24689
22. Song HK, Yan L, Smith RX, et al. Noncontrast enhanced four-dimensional dynamic MRA with golden angle radial acquisition and K-space weighted image contrast (KWIC) reconstruction. *Magn Reson Med*. Dec 2014;72(6):1541-51. doi:10.1002/mrm.25057
23. Wu H, Block WF, Turski PA, et al. Noncontrast dynamic 3D intracranial MR angiography using pseudo-continuous arterial spin labeling (PCASL) and accelerated 3D radial acquisition. *J Magn Reson Imaging*. May 2014;39(5):1320-6. doi:10.1002/jmri.24279
24. Kopeinigg D, Bammer R. Time-resolved angiography using inflow subtraction (TRAILS). *Magn Reson Med*. Sep 2014;72(3):669-78. doi:10.1002/mrm.24985
25. Chen L, Mossa-Basha M, Sun J, et al. Quantification of morphometry and intensity features of intracranial arteries from 3D TOF MRA using the intracranial artery feature extraction (iCafe): A reproducibility study. *Magn Reson Imaging*. Apr 2019;57:293-302. doi:10.1016/j.mri.2018.12.007
26. Chen L, Sun J, Hippe DS, et al. Quantitative assessment of the intracranial vasculature in an older adult population using iCafe. *Neurobiol Aging*. Jul 2019;79:59-65. doi:10.1016/j.neurobiolaging.2019.02.027
27. Uchiyama Y, Yamauchi M, Ando H, et al. Automated classification of cerebral arteries in MRA images and its application to maximum intensity projection. *Conf Proc IEEE Eng Med Biol Soc*. 2006;2006:4865-8. doi:10.1109/IEMBS.2006.260438
28. Bogunovic H, Pozo JM, Cardenes R, San Roman L, Frangi AF. Anatomical labeling of the Circle of Willis using maximum a posteriori probability estimation. *IEEE Trans Med Imaging*. Sep 2013;32(9):1587-99. doi:10.1109/TMI.2013.2259595
29. Bilgel M, Roy S, Carass A, Nyquist PA, Prince JL. Automated anatomical labeling of the cerebral arteries using belief propagation. *Proc SPIE Int Soc Opt Eng*. Mar 13 2013;866918doi:10.1117/12.2006460
30. Bullitt E, Zeng D, Gerig G, et al. Vessel tortuosity and brain tumor malignancy: a blinded study. *Acad Radiol*. Oct 2005;12(10):1232-40. doi:10.1016/j.acra.2005.05.027
31. Bogunovic H, Pozo JM, Cardenes R, Frangi AF. Automatic identification of internal carotid artery from 3DRA images. *Annu Int Conf IEEE Eng Med Biol Soc*. 2010;2010:5343-6. doi:10.1109/IEMBS.2010.5626473
32. Bogunovic H, Pozo JM, Cardenes R, Frangi AF. Anatomical labeling of the anterior circulation of the Circle of Willis using maximum a posteriori classification. *Med Image Comput Comput Assist Interv*. 2011;14(Pt

3):330-7. doi:10.1007/978-3-642-23626-6_41

33. Robben D, Turetken E, Sunaert S, et al. Simultaneous segmentation and anatomical labeling of the cerebral vasculature. *Med Image Anal*. Aug 2016;32:201-15. doi:10.1016/j.media.2016.03.006

34. Girard F, Kavalec C, Cheriet F. Joint segmentation and classification of retinal arteries/veins from fundus images. *Artif Intell Med*. Mar 2019;94:96-109. doi:10.1016/j.artmed.2019.02.004

35. Wolterink JM LT, I Išgum. Graph convolutional network for coronary artery segmentation in cardiac CT angiography. presented at: International Workshop on Graph Learning in Medical Imaging; 2019;

36. Chen L, Mossa-Basha M, Balu N, et al. Development of a quantitative intracranial vascular features extraction tool on 3D MRA using semiautomated open-curve active contour vessel tracing. *Magn Reson Med*. Jun 2018;79(6):3229-3238. doi:10.1002/mrm.26961

37. Gaha M, Roy C, Estrade L, et al. Inter- and intraobserver agreement in scoring angiographic results of intra-arterial stroke therapy. *AJNR Am J Neuroradiol*. Jun 2014;35(6):1163-9. doi:10.3174/ajnr.A3828

38. Butler T, Zaborszky L, Pirraglia E, et al. Comparison of human septal nuclei MRI measurements using automated segmentation and a new manual protocol based on histology. *Neuroimage*. Aug 15 2014;97:245-51. doi:10.1016/j.neuroimage.2014.04.026

39. Koerte I, Haberl C, Schmidt M, et al. Inter- and intra-rater reliability of blood and cerebrospinal fluid flow quantification by phase-contrast MRI. *J Magn Reson Imaging*. Sep 2013;38(3):655-62. doi:10.1002/jmri.24013